

Kinetic Alfvén waves generation by large-scale phase-mixing

C. L. Vásconez^{1,2}, F. Pucci¹, F. Valentini¹, S. Servidio¹, W. H. Matthaeus³, F. Malara¹

¹Dipartimento di Fisica, Università della Calabria, 87036, Rende (CS), Italy.

²Observatorio Astronómico de Quito, Escuela Politécnica Nacional, Quito, Ecuador.

³Department of Physics and Astronomy, University of Delaware, DE 19716, USA.

Received _____; accepted _____

ABSTRACT

One view of the solar-wind turbulence is that the observed highly anisotropic fluctuations at spatial scales near the proton inertial length d_p may be considered as Kinetic Alfvén waves (KAWs). In the present paper, we show how phase-mixing of large-scale parallel propagating Alfvén waves is an efficient mechanism for the production of KAWs at wavelengths close to d_p and at large propagation angle with respect to the magnetic field. Magnetohydrodynamic (MHD), Hall-Magnetohydrodynamic (HMHD), and hybrid Vlasov-Maxwell (HVM) simulations modeling the propagation of Alfvén waves in inhomogeneous plasmas are performed. In linear regime, the role of dispersive effects is singled out by comparing MHD and HMHD results. Fluctuations produced by phase-mixing are identified as KAWs through a comparison of polarization of magnetic fluctuations and wave group velocity with analytical linear predictions. In the nonlinear regime, comparison of HMHD and HVM simulations allows to point out the role of kinetic effects in shaping the proton distribution function. We observe generation of temperature anisotropy with respect to the local magnetic field and production of field-aligned beams. The regions where the proton distribution function highly departs from thermal equilibrium are located inside the shear layers, where the KAWs are excited, this suggesting that the distortions of the proton distribution are driven by a resonant interaction of protons with KAW fluctuations. Our results are relevant in configurations where magnetic field inhomogeneities are present, as, for example, in the solar corona where the presence of Alfvén waves has been ascertained.

Subject headings:

1. Introduction

Turbulence in plasmas is a complex phenomenon which is characterized by different regimes in different ranges of spatial and temporal scales. Turbulence in the solar wind has been extensively studied, both by detailed analyses of in-situ measurements and from a theoretical point of view; see Bruno & Carbone (2005) for a review. Such studies often adopt complementary views that the turbulence may be described either as collection of wave that interact nonlinearly, so-called wave-turbulence, or else as a collection of broad band, essentially zero frequency eddies or flux tubes that form a hierarchy of coherent structures. These approaches have been extensively reviewed (Barnes 1979; Matthaeus et al. 2015) and we do not attempt a critical comparison in the present work. Instead, we adopt mainly a wave taxonomy of the fluctuations, based on linear theory in order to address a specific set of questions. As motivation, we note that a variety of observations in the solar wind (Bale et al. 2005; Sahraoui et al. 2009) have suggested that fluctuations near the end of the magnetohydrodynamics inertial cascade range, and approaching the kinetic plasma range, may consist primarily of Kinetic Alfvén waves (KAWs). Here we address in particular the nature of fluctuations produced due to nonlinear interactions near the proton inertial length d_p and investigate in some detail the basis for identifying them as KAWs. We show how phase-mixing of large-scale parallel propagating Alfvén waves is an efficient mechanism for the production of KAWs at wavelengths close to d_p and at large propagation angle with respect to the magnetic field. To support the interpretation as KAWs, we perform and analyze Magnetohydrodynamic (MHD), Hall-Magnetohydrodynamic (HMHD), and hybrid Vlasov-Maxwell (HVM) simulations that model the propagation of Alfvén waves and their fully nonlinear interaction with a nonuniform plasma background. We will be able to characterize fluctuations produced by this “phase-mixing-”like interaction as highly oblique KAWs.

At frequencies much lower than the proton gyrofrequency, solar wind turbulence is dominated by Alfvénic fluctuations, which are characterized by highly-correlated velocity and magnetic fields and by low-level (with respect to the background values) density and magnetic field intensity variations (Belcher & Davis 1971). Moreover, in recent years several indications have been found of the presence of Alfvén waves also in the solar corona (Tomczyk et al. 2007; Tomczyk & McIntosh 2009) from where the solar wind emanates. In the solar wind, Alfvénic fluctuations extend over a wide range of spatial scales, from large scales within the MHD range, down to lengths comparable or smaller than the proton inertial length d_p , where also finite Larmor radius effects become relevant. Moreover, in this scenario it is important to take into account the role of spectral anisotropy. Theoretical studies, indeed, have shown that in a MHD turbulence the energy cascade preferentially takes place perpendicularly to the background magnetic field \mathbf{B}_0 (e.g., Shebalin et al. (1983); Carbone & Veltri (1990); Oughton et al. (1994)). Then, it is expected that at smaller scales the fluctuation energy tends to concentrate in nearly perpendicular wavevectors. This idea is supported by observational data showing that the distribution of wavevectors of magnetic fluctuations has a significant population quasi-perpendicular to the ambient magnetic field (Matthaeus et al. 1986, 1990). All the above effects, such as turbulence in a plasma with several characteristic lengthscales, Alfvénic correlations and spectral anisotropy, can interact with large scale structures such as shears and magnetic equilibria, with a subsequent generation of wave-like activity. The full picture need to be addressed with plasma simplified models, as well as the Vlasov-Maxwell treatment.

Waves belonging to the Alfvén branch, with wavelengths comparable with the proton inertial length d_p and wavevectors nearly perpendicular to the mean magnetic field \mathbf{B}_0 are often indicated as “kinetic Alfvén waves”. During the last decades, KAWs have received considerable attention and have been studied in detail due to their possible role in a wave description of the turbulent cascade. Since the MHD cascade favors nearly

perpendicular wavevectors, the expectation within a wave perspective would be that KAWs are naturally present at scales of the order of d_p . An extensive analysis of KAW physics is found in Hollweg (1999) (see also references therein for a more complete view on the subject). Many solar wind observational analyses (Bale et al. 2005; Sahraoui et al. 2009; Podesta & Tenbarge 2012; Salem et al. 2012; Chen et al. 2013; Kiyani et al. 2013), theoretical works (Howes et al. 2008a; Schekochihin et al. 2009; Sahraoui et al. 2012) as well as numerical simulations (Gary & Nishimura 2004; Howes et al. 2008b; TenBarge & Howes 2012) have suggested that KAWs can play an important role in the dissipation of turbulent energy. Due to a nonvanishing electric field parallel component associated with KAWs, these waves have also been considered in the problem of particle acceleration (Voitenko & Goossens 2004; Décamp & Malara 2006). Recently, Váscquez et al. (2014) have studied collisionless Landau damping and wave-particle resonant interactions in KAWs.

There are also simplified problems, less complex than fully developed turbulence, in which one finds the formation of small scales in the direction perpendicular to an applied magnetic field \mathbf{B}_0 . It is well known that this effect appears in the context of MHD when imposed parallel propagating waves interact with an inhomogeneous background consisting either of pressure balanced structures or velocity shears (Ghosh et al. 1998). In 2D equilibria, where the Alfvén velocity varies in directions perpendicular to the magnetic field, two mechanisms have been investigated in detail: (1) phase-mixing (Heyvaerts & Priest 1983), in which differences in group velocity at different locations progressively bend wavefronts; and (2) resonant absorption which concentrates the wave energy in a narrow layer where the wave frequency locally matches a characteristic frequency (Alfvén or cusp). These processes have been studied both by investigating normal modes of the inhomogeneous structure (Kappraff & Tataronis 1977; Mok & Einaudi 1985; Steinolfson 1985; Davila 1987; Hollweg 1987; Califano et al. 1990, 1992) and by considering the

evolution of an initial disturbance (Lee & Roberts 1986; Malara et al. 1992, 1996). Effects of density stratification and magnetic line divergence (Ruderman et al. 1998), as well as nonlinear coupling with compressive modes (Nakariakov et al. 1997, 1998), and evolution of localized pulses (Tsiklauri & Nakariakov 2002; Tsiklauri et al., 2003) have been considered. The propagation of MHD waves in inhomogeneous magnetic fields containing null points has also been studied in detail (Landi et al. (2005); see also McLaughlin et al. (2010) for a review). Phase-mixing in 3D inhomogeneous equilibria has also been considered in the small wavelength limit (Similon & Sudan 1989) using a WKB approximation (Petkaki et al. 1998; Malara et al. 2000), also within the problem of coronal heating (Malara et al. 2003, 2005, 2007). Particle acceleration in phase-mixing of Alfvén waves in a dispersive regime has been studied by Tsiklauri et al. (2005) using particle-in-cell simulations, both in 2D (Tsiklauri 2011) and in 3D (Tsiklauri 2012) configurations. Finally, instabilities generating KAWs in plasma with transverse density modulations have been considered by Wu & Chen (2013). Similar ideas involving dissipative mechanisms related to interaction of Alfvén waves or KAWs and phase-mixing have been examined in the context of the magnetospheric plasma sheet (Lysak & Song 2011) and in coronal loops (Ofman & Aschwanden 2002).

The above considerations suggest that phase-mixing of Alfvén waves might represent a mechanism to produce KAWs, when the wavelength of waves becomes enough small to be comparable with the proton inertial length d_p . This effect could work, for instance, in the solar corona where the background magnetic field is clearly inhomogeneous and where the presence of Alfvén waves has been ascertained. This represents an indication about the nature of small-scale fluctuations that could be present in the coronal plasma. The aim of the present paper is to investigate directly the generation of KAW fluctuations associated with Alfvén wave phase-mixing. This study will be performed numerically by using both a HMHD code and a Vlasov-hybrid code. The former include proton skin depth effects, while the latter allows identification of kinetic effects such as wave-particle resonances

and temperature anisotropy. In Section 2 the model will be presented along with a linear analysis of wave properties; the results derived by the HMHD in the linear regime are described in Section 3, while the nonlinear regime and the results of the Vlasov-hybrid code will be described in Section 4; a discussion and a summary of results are given in Section 5.

2. Hall-MHD model

Consider a fluid plasma composed of protons and electrons. For phenomena at sufficiently large scales the electron mass can be neglected $m_e \ll m_p$ and the quasi-neutrality condition holds: $n_e \simeq n_p$, with n_e and n_p the number densities of electrons and protons, respectively. Moreover, we assume that the temperatures of protons and electrons are equal $T_e = T_p = T$. Finally, the displacement current term is neglected in the Ampere equation. In these conditions the plasma dynamics can be described by the HMHD equations:

$$\frac{\partial \rho}{\partial t} + \nabla \cdot (\rho \mathbf{v}) = 0 \quad (1)$$

$$\frac{\partial \mathbf{v}}{\partial t} + (\mathbf{v} \cdot \nabla) \mathbf{v} = -\frac{\tilde{\beta}}{2\rho} \nabla(\rho T) + \frac{1}{\rho} [(\nabla \times \mathbf{B}) \times \mathbf{B}] \quad (2)$$

$$\frac{\partial \mathbf{B}}{\partial t} = \nabla \times \left[\mathbf{v} \times \mathbf{B} - \frac{\tilde{\epsilon}}{\rho} (\nabla \times \mathbf{B}) \times \mathbf{B} \right] \quad (3)$$

$$\frac{\partial T}{\partial t} + (\mathbf{v} \cdot \nabla) T + (\gamma - 1) T (\nabla \cdot \mathbf{v}) = 0 \quad (4)$$

Equations (1)-(4) contain only dimensionless quantities. In particular, mass density ρ (which is only due to protons) is normalized to a typical density $\tilde{\rho}$, temperature T to a typical value \tilde{T} , the pressure $p = \rho T$ due to both protons and electrons is normalized to the value $\tilde{p} = 2\kappa_B \tilde{\rho} \tilde{T} / m_p$, with κ_B the Boltzmann constant and m_p the proton mass. The spatial coordinates are normalized to a typical length \tilde{L} , magnetic field \mathbf{B} is normalized to a typical magnetic field \tilde{B} , fluid velocity \mathbf{v} to the typical Alfvén speed $\tilde{c}_A = \tilde{B} / (4\pi \tilde{\rho})^{1/2}$, time t to the Alfvén time $\tilde{t}_A = \tilde{L} / \tilde{c}_A$. Finally, the plasma beta $\tilde{\beta} = \tilde{p} / (\tilde{B}^2 / 8\pi)$ is a typical value

for the kinetic to magnetic pressure ratio; $\gamma = 5/3$ is the adiabatic index; $\tilde{\epsilon} = \tilde{d}_p/\tilde{L} \ll 1$ is the Hall parameter measuring the relative amplitude of the Hall term with respect to the $\mathbf{v} \times \mathbf{B}$ term in the Ohm's law, $\tilde{d}_p = \tilde{c}_A/\tilde{\Omega}_{cp} = \tilde{c}_A m_p c / (q\tilde{B})$ being the proton inertial length. Equations (1)-(4) reduce to the ordinary single fluid compressible MHD equations in the limit $\tilde{\epsilon} \rightarrow 0$. The equations are ideal and adiabatic due to the absence of viscosity in Eq. (2), resistivity in Eq. (3) and heat sources and heat conduction in Eq. (4). For the simulations carried out below these effects are present in some form (not necessarily in the form of a fluid model); however at present they are omitted for clarity.

2.1. Wave properties

We consider first a uniform equilibrium state characterized by homogeneous dimensionless density ρ_0 , temperature T_0 , magnetic field \mathbf{B}_0 and vanishing velocity $\mathbf{v}_0 = 0$. Waves propagating in the above equilibrium can be studied as usual: a small amplitude perturbation is superposed on the equilibrium; equations (1)-(4) are linearized with respect to the perturbation amplitude and perturbation fields are Fourier transformed both in space and time. Imposing nonvanishing perturbations leads to the following dispersion relation:

$$\omega^6 + C_1\omega^4 + C_2\omega^2 + C_3 = 0 \quad (5)$$

with

$$C_1 = -k_{\parallel}^2 (2c_{A0}^2 + c_{s0}^2) - k_{\perp}^2 (c_{A0}^2 + c_{s0}^2) - \frac{c_{A0}^4 k_{\parallel}^2 (k_{\parallel}^2 + k_{\perp}^2)}{\omega_{p0}^2} \quad (6)$$

$$C_2 = c_{A0}^2 k_{\parallel}^2 (c_{A0}^2 + 2c_{s0}^2) (k_{\parallel}^2 + k_{\perp}^2) + \frac{c_{A0}^4 c_{s0}^2 k_{\parallel}^2 (k_{\parallel}^4 + 2k_{\parallel}^2 k_{\perp}^2 + k_{\perp}^4)}{\omega_{p0}^2} \quad (7)$$

$$C_3 = -c_{A0}^4 c_{s0}^2 k_{\parallel}^4 (k_{\parallel}^2 + k_{\perp}^2) \quad (8)$$

In equations, (5)-(8) ω is the wave frequency normalized to \tilde{t}_A^{-1} ; k_{\parallel} and k_{\perp} are the wavevector components parallel and perpendicular to \mathbf{B}_0 , respectively, both normalized to

\tilde{L}^{-1} ; $c_{A0} = B_0/(4\pi\rho_0)^{1/2}$ and $c_{s0} = (\tilde{\beta}\gamma T_0/2)^{1/2}$ are the Alfvén speed and the sound speed associated with the equilibrium, respectively; $\omega_{p0} = (q\tilde{B}B_0/(m_p c))(\tilde{L}/\tilde{c}_A)$ is the normalized proton gyrofrequency. The squared sound speed to Alfvén speed ratio will be indicated by $\beta_0 = c_{s0}^2/c_{A0}^2$.

The expressions (5)-(8) are equivalent to those found in a two-fluid model by Vázquez et al. (2014) if the electron inertia is neglected. Equation (5) has been analytically solved (Vázquez et al. 2014) using the Vieta’s substitution method (Birkhoff & Mac Lane 1977) for the calculation of the complex roots of a third-degree algebraic equation. For given values of k_{\parallel} and k_{\perp} the three solutions found for ω^2 are real and positive and correspond to the Alfvén, fast magnetosonic (FM) and slow magnetosonic (SM) branches, respectively. In particular, KAWs correspond to the Alfvén branch for $k_{\parallel} \ll k_{\perp} \sim \omega_{p0}/c_{A0}$.

From the linear analysis the expressions for the amplitudes of fluctuations can be calculated. We use a reference frame where the x -axis is along \mathbf{B}_0 while the wavevector \mathbf{k} is in the xy plane. The perturbation components for a wave with wavevector $\mathbf{k} = k_{\parallel}\mathbf{e}_x + k_{\perp}\mathbf{e}_y$ can be expressed in the following form:

$$v_{1x} = a \frac{c_{A0}^2 c_{s0}^2 k_{\parallel} k_{\perp} \omega_{p0}}{\omega^2 (\omega^2 - c_{s0}^2 k^2)} \left(1 - \frac{\omega^2}{c_{A0}^2 k_{\parallel}^2} \right) \sin(k_{\parallel}x + k_{\perp}y - \omega t + \phi) \quad (9)$$

$$v_{1y} = a \frac{c_{A0}^2 k_{\parallel} \omega_{p0} (\omega^2 - c_{s0}^2 k_{\parallel}^2)}{\omega^2 (\omega^2 - c_{s0}^2 k^2)} \left(1 - \frac{\omega^2}{c_{A0}^2 k_{\parallel}^2} \right) \sin(k_{\parallel}x + k_{\perp}y - \omega t + \phi) \quad (10)$$

$$v_{1z} = -a \frac{c_{A0}^2 k_{\parallel}}{\omega} \cos(k_{\parallel}x + k_{\perp}y - \omega t + \phi) \quad (11)$$

$$B_{1x} = aB_0 \frac{k_{\parallel} k_{\perp} \omega_{p0}}{\omega k^2} \left(1 - \frac{\omega^2}{c_{A0}^2 k_{\parallel}^2} \right) \sin(k_{\parallel}x + k_{\perp}y - \omega t + \phi) \quad (12)$$

$$B_{1y} = -aB_0 \frac{k_{\parallel}^2 \omega_{p0}}{\omega k^2} \left(1 - \frac{\omega^2}{c_{A0}^2 k_{\parallel}^2} \right) \sin(k_{\parallel}x + k_{\perp}y - \omega t + \phi) \quad (13)$$

$$B_{1z} = aB_0 \cos(k_{\parallel}x + k_{\perp}y - \omega t + \phi) \quad (14)$$

where a is the perturbation amplitude, $\phi \in [0, 2\pi]$ is the phase and $\omega = \omega(\mathbf{k})$ is derived from the dispersion relation (5).

In what follows it will be useful to have an expression for the component of the wave group velocity perpendicular to \mathbf{B}_0 , $v_{g\perp} = \partial\omega/\partial k_\perp$. This has been calculated in the following way: we indicate by $F(\omega, k_\parallel, k_\perp)$ the LHS of equation (5) and by $\omega(k_\parallel, k_\perp)$ a solution of equation (5). Substituting $\omega(k_\parallel, k_\perp)$ in the place of ω into equation (5) we obtain an identity

$$F(\omega(k_\parallel, k_\perp), k_\parallel, k_\perp) \equiv 0 \quad (15)$$

which holds for any value of k_\parallel and k_\perp . The derivative of equation (15) with respect to k_\perp is

$$\frac{dF}{dk_\perp} = \frac{\partial F}{\partial \omega} \frac{\partial \omega}{\partial k_\perp} + \frac{\partial F}{\partial k_\perp} = 0$$

from which we obtain

$$v_{g\perp} = \frac{\partial \omega}{\partial k_\perp} = -\frac{\partial F/\partial k_\perp}{\partial F/\partial \omega} \quad (16)$$

The derivatives of F appearing in the RHS of equation (16) can be calculated using equations (5)-(8); their expressions are:

$$\begin{aligned} \frac{\partial F}{\partial k_\perp} = & -2 \left[k_\perp (c_{A0}^2 + c_{s0}^2) + \frac{k_\perp k_\parallel^2 c_{A0}^4}{\omega_{p0}^2} \right] \omega^4 + \\ & 2 \left[k_\perp k_\parallel^2 (2c_{s0}^2 c_{A0}^2 + c_{A0}^4) + 2 \frac{(k_\perp k_\parallel^4 + k_\perp^3 k_\parallel^2) c_{A0}^4 c_{s0}^4}{\omega_{p0}^2} \right] \omega^2 - 2k_\perp k_\parallel^4 c_{s0}^2 c_{A0}^4 \quad (17) \end{aligned}$$

$$\begin{aligned} \frac{\partial F}{\partial \omega} = & 6\omega^5 - 4 \left[k^2 (c_{A0}^2 + c_{s0}^2) + k_\parallel^2 c_{A0}^2 + \frac{k^2 k_\parallel^2 c_{A0}^2}{\omega_{p0}^4} \right] \omega^3 + \\ & 2 \left[k^2 k_\parallel^2 (2c_{s0}^2 c_{A0}^2 + c_{A0}^4) + \frac{k_\parallel^2 k^4 c_{A0}^4 c_{s0}^2}{\omega_{p0}^2} \right] \omega \quad (18) \end{aligned}$$

where $k^2 = k_\parallel^2 + k_\perp^2$. Since phase-mixing increases k_\perp leaving k_\parallel constant (as shown in the following section), in Fig. 1 the perpendicular group velocity $v_{g\perp}$ of the Alfvén, FM and SM

modes is plotted as a function of k_{\perp} in a range $k_{\perp} \geq k_{\parallel}$, for $k_{\parallel} = 1$ and for $\beta_0 = 1.25$ and $\beta_0 = 2.08$. The choice of these two values of β_0 will be justified in the next section. From Fig. 1 we see that $v_{g\perp}$ of the three modes increases with increasing k_{\perp} , becoming nearly constant at large propagation angles. For $k_{\perp} \geq k_{\parallel} = 1$, $v_{g\perp}$ is positive for Alfvén and FM waves while is negative for SM waves. Moreover, $v_{g\perp}$ of FM waves is much larger than that of the Alfvén branch; this is consistent with a quasi-isotropic propagation velocity of FM waves. The behavior of $v_{g\perp}$ for negative k_{\perp} can be inferred from Fig. 1 taking into account that $v_{g\perp}(k_{\parallel}, -k_{\perp}) = -v_{g\perp}(k_{\parallel}, k_{\perp})$. These features will be used to identify the nature of fluctuations generated by phase-mixing.

3. MHD and Hall-MHD simulations of phase-mixing

We consider a 2.5D configuration where all the physical quantities depend only on two spatial variables (x and y), but vector quantities can have three nonvanishing components. The above quantities are defined in a spatial domain $D = \{(x, y)\} = [0, 2\pi] \times [0, 2\pi]$ (in dimensionless units), where periodic boundary conditions are imposed both in the x and y directions. We consider a nonuniform equilibrium structure in D , where physical quantities vary only along the y -direction, or are uniform. Quantities relative to the equilibrium are indicated by the upper index "(0)". The equilibrium magnetic field is

$$\mathbf{B}^{(0)} = B^{(0)}(y)\mathbf{e}_x \quad (19)$$

where

$$B^{(0)}(y) = 1 + \frac{b_m - 1}{1 + \left(\frac{y - \pi}{2\pi h}\right)^r} + \alpha \left(\frac{y}{\pi} - 1\right)^2 \quad (20)$$

and \mathbf{e}_x is the unit vector along x . The dimensionless parameters in the expression (20) have the following values: $b_m = 1.5$, $h = 0.2$, $r = 10$ and

$$\alpha = \frac{(b_m - 1)r}{2(2h)^r \left[1 + \left(\frac{1}{2h} \right)^r \right]^2} \simeq 2.62 \times 10^{-4} \quad (21)$$

The function $B^{(0)}(y)$ is symmetrical with respect to the central point $y = \pi$, where it reaches its maximum value b_m . The small term containing α in the expression (20) has been added in order to have a vanishing first derivative of $B^{(0)}(y)$ at the two boundaries $y = 0$ and $y = 2\pi$. Both $B^{(0)}(y)$ and $dB^{(0)}/dy$ are periodic functions in the interval $[0, 2\pi]$. However, higher order derivatives of $B^{(0)}(y)$ are not exactly periodic; as a consequence, the Fourier spectrum of $B^{(0)}(y)$ has a tail at high wavenumbers. To avoid this drawback, the expression (20) has been corrected by filtering out harmonics with wavenumbers larger than 70 in its spectrum. The filter does not sensibly alter the profile $B^{(0)}(y)$. The equilibrium magnetic field is almost constant both in the central half and on the two lateral parts of the domain, while two sharp shear layers (current sheets) are located in between these uniform regions. The equilibrium temperature, which is equal both for protons and electrons, has been chosen as uniform, while the fluid velocity is identically zero:

$$T^{(0)} = 1 \quad , \quad \mathbf{v}^{(0)} = 0 \quad (22)$$

The equilibrium mass density $\rho^{(0)}(y)$ is determined by total pressure equilibrium:

$$\frac{\tilde{\beta}}{2} \rho^{(0)}(y) T^{(0)} + \frac{B^{(0)2}(y)}{2} = P_T^{(0)} \quad (23)$$

where $P_T^{(0)} = 1.748$ and $\tilde{\beta} = 2$. The Alfvén and sound velocities associated with equilibrium structure are given by $c_A^{(0)}(y) = B^{(0)}(y)/[\rho^{(0)}(y)]^{1/2}$ and $c_s^{(0)} = (\tilde{\beta}\gamma T^{(0)}/2)^{1/2}$, respectively. The local plasma β is $\beta^{(0)}(y) = [c_s^{(0)}/c_A^{(0)}(y)]^2$. The profiles of $c_A^{(0)}(y)$ and $\beta^{(0)}(y)$ are shown in Fig. 2. The Alfvén velocity is larger in the lateral parts of D than in the center; the inhomogeneity of $c_A^{(0)}$ is responsible for phase-mixing of Alfvén waves. We note that $\beta^{(0)} < 1$

in the central region, while $\beta^{(0)}$ becomes larger than 1 when approaching the boundaries $y = 0$ and $y = 2\pi$. In particular, $\beta^{(0)} = 1.25$ in the middle of the shear layers while $\beta^{(0)} = 2.08$ in the lateral homogeneous regions; these two values have been used to calculate the profiles of Figs 1 and 5.

At the initial time an Alfvénic perturbation has been superposed on the above equilibrium. Quantities relative to the perturbation are indicated by the upper index "1". The initial magnetic field and velocity perturbation are given by

$$\mathbf{B}^{(1)}(x, y, t = 0) = a \cos(x) \mathbf{e}_z \quad , \quad \mathbf{v}^{(1)}(x, y, t = 0) = -a[\rho^{(0)}(y)]^{-1/2} \cos(x) \mathbf{e}_z \quad (24)$$

so that $\mathbf{v}^{(1)} = -(c_A^{(0)}/B^{(0)})\mathbf{B}^{(1)}$. The quantity a gives the amplitude of the initial perturbation. Initial density and temperature fluctuations are vanishing: $\rho^{(1)}(x, y, t = 0) = 0$, $T^{(1)}(x, y, t = 0) = 0$.

The MHD case is described by equations (1)-(4) with $\tilde{\epsilon} = 0$. In this case and in the small-amplitude limit $a \ll 1$ the equations may be linearized and above initial conditions evolve in time according to the equations:

$$\mathbf{B}^{(1)}(x, y, t) = a \cos \left[x - c_A^{(0)}(y)t \right] \mathbf{e}_z \quad , \quad \mathbf{v}^{(1)}(x, y, t) = -a[\rho^{(0)}(y)]^{-1/2} \cos \left[x - c_A^{(0)}(y)t \right] \mathbf{e}_z \quad (25)$$

indicating that the initial perturbation propagates along $\mathbf{B}^{(0)}$ at the local Alfvén speed. Thus, transverse variations of $c_A^{(0)}$ generates in the perturbation increasingly smaller scales which are localized within the shear layers. This phenomenon represents phase-mixing of an Alfvén wave (Heyvaerts & Priest 1983).

The fully nonlinear equations (1)-(4) have been solved numerically with the above-specified boundary and initial conditions. The HMHD numerical code employs a 2D Fourier pseudospectral method to calculate spatial derivatives and time integration is performed via a second-order Runge-Kutta scheme. Aliasing errors in the evaluation of nonlinear terms

are partially removed by a 2/3 truncation in the spectral space. Equations have been solved using the scheme described in Ghosh et al. (1993). Hyper-viscosity and hyper-resistivity terms (fourth-order derivatives) have been added in equations (2) and (3) in order to obtain numerical stability with dissipation concentrated only at the smallest spatial scales.

Different runs have been performed; Table 1 summarizes the values of parameters used in the various cases, with n_x and n_y the number of gridpoints in the x and y direction. RUN 1 corresponds to the MHD case ($\tilde{\epsilon} = 0$) with a low-amplitude perturbation ($a = 0.01$). Though the analytical solution for an infinitesimal amplitude is known (equations (25)), we performed this run to single out differences of a purely MHD case with respect to a HMHD case ($\tilde{\epsilon} \neq 0$). Fluctuating fields are defined as $\delta g = g - \langle g \rangle_x$, where g represents a physical quantity from which the spatial average along x has been subtracted in order to eliminate the contribution from the equilibrium structure. The effect of phase-mixing is visible in the time evolution of δv_z and δB_z (not shown): the wave propagates from left to right but with a velocity which is larger in the central part than in the lateral parts of the domain. As a consequence, within the two shear layers the wave profile is stretched with small-scale gradients generated in the transverse (y) direction. The other components of $\delta \mathbf{v}$ and $\delta \mathbf{B}$, as well as the density and temperature fluctuations, have a much lower amplitude which is of the order of 10^{-4} , or smaller. Moreover, these fluctuations have a wavelength in the x direction which is half of the wavelength of δv_z and δB_z . These two features clearly indicate that in the MHD case δv_x , δv_y , δB_x , δB_y , $\delta \rho$ and δT are generated by small nonlinear effects that are quadratic in the Alfvén wave amplitude.

In RUN 2 we considered again a small-amplitude initial wave ($a = 0.01$), but now dispersive effects have been switched on by setting the coefficient of the Hall term $\tilde{\epsilon} = 0.125$. This corresponds to set the proton inertial length $\tilde{d}_p = 0.125$ (in normalized units). Thus, it is expected that dispersive effects are no longer negligible as soon as the perturbation

wavevector k has increased enough (in consequence of phase-mixing) to become comparable with \tilde{d}_p^{-1} . This condition is reached inside the shear layers. The time t_d at which $k \sim \tilde{d}_p^{-1}$ can be estimated in the following way: during phase-mixing the transverse wavevector component k_y increases in time according to the equation (e.g. Petkaki et al. (1998))

$$k_y(t) \sim k_{y0} - \left(\frac{dc_{A0}}{dy} \right)_s k_x t \quad (26)$$

where $(dc_{A0}/dy)_s$ is an estimation of the Alfvén velocity gradient in the shear layers, while k_x is constant and $k_{y0} = k_y(t = 0)$. In our case $k_x = 1$, $k_{y0} = 0$ and $(dc_{A0}/dy)_s \simeq -1$ (in the shear layer at $x \simeq 4.5$). At the time $t = t_d$ we have $k_y \gg k_x$; then, from the condition $k_y(t_d)d_p \simeq 1$ we get the estimate

$$t_d \simeq -\frac{1}{d_p k_x \left(\frac{dc_{A0}}{dy} \right)_s} \simeq 8 \quad (27)$$

In our configuration it is expected that at times $t \gtrsim t_d$ phase-mixing could generate KAWs, i.e., perturbations belonging to the Alfvén branch with a quasi-perpendicular wavevector ($k_y \gg k_x$). We now explore this possibility in some detail.

In Fig. 3 the fluctuating fields $\delta\rho$, δT , $\delta\mathbf{v}$ and $\delta\mathbf{B}$ are represented at the time $t = 13.1$, along with the current density component j_z which has been plotted in order to localize the equilibrium shear layers. The time $t = 13.1$ is larger than t_d , thus we expect to observe effects due to finite ion inertial length. We observe that δv_x , δB_x , $\delta\rho$ and δT are now of the same order as δv_z and δB_z and the parallel wavelength is 2π for all these fields. This indicates that in the HMHD case δv_x , δB_x , $\delta\rho$ and δT fluctuations are not due to nonlinear effects but they are part of the same perturbation as δv_z and δB_z , namely, a KAW. A clearer identification of this perturbation as a KAW will be given in the following.

In Section 2.1 we found that the perpendicular group velocity of KAWs is nonvanishing, though it is much smaller than the background Alfvén velocity. Then, in the present

configuration, KAWs generated inside the shear layers, while propagating along $\mathbf{B}^{(0)}$, slowly drift in the y direction. The perpendicular group velocity $v_{g\perp}$ of KAWs has the same sign as $k_y = k_\perp$ (see Fig. 1), the latter being negative (positive) in the shear layer located at $y \simeq 1.8$ ($y \simeq 4.5$). Then, KAWs produced in both shear layers would move outside toward the lateral higher- $\beta^{(0)}$ uniform regions. Indeed, examining the time behavior of the perturbation, oblique wavefronts progressively occupying the two lateral regions are found. This behavior can be seen in Fig. 4 where the δB_x component is plotted at four different times. We used the following procedure to measure the propagation of these structures in the direction perpendicular to $\mathbf{B}^{(0)}$.

Once the system undergoes phase-mixing, and once wavepackets are generated (at about $t \sim 3$), we identify all the local maxima and minima of the density field ρ (different fields give similar results). In practice, following Donato et al. (1998), all the critical points \mathbf{x}_* where $\nabla\rho = 0$ have been found. In these points we computed the square Hessian matrix of ρ , identifying the strongest maxima and minima. We followed the trajectories of these points in time (which are almost parallel each other), that go from the shear layer out to the border. Taking the average position between the maximum and the minimum, we calculated its velocity, obtaining $u_y \simeq \pm 5.4 \times 10^{-2}$. We can also estimate their wavevector components $k_y = \pm 2\pi/\lambda_y \simeq \pm 8.11$ and $k_x = 1$. Using these values in the expression (16) we obtain for the perpendicular group velocity of the Alfvén branch (see Figs 1 and 2) the value $v_{g\perp} = \pm 7.1 \times 10^{-2}$ for $\beta^{(0)} = 2.08$ (in the lateral homogeneous region), in reasonable agreement with the value u_y estimated in the simulation. We conclude that the observed structures propagate with the group velocity of KAWs. We note also that the propagation angle is $\theta = \arctan |k_y/k_x| \simeq 83^\circ$, close to $\pi/2$ as required for KAWs.

From Fig. 1 we note that $v_{g\perp}$ is opposite to k_\perp for waves belonging to the SM branch. This implies that SM waves possibly produced in the shear layers would laterally drift

opposite to KAWs. Thus, the waves observed in the lateral homogeneous region cannot belong to the SM mode. Finally, Fig. 1 indicates that for large propagation angles the group velocity of FM waves is much larger than that of KAWs, being $\simeq 1.8$ for the above values of k_x and k_y . This value is much larger than the lateral propagation velocity u_y of the observed perturbation. Consequently, the fluctuation produced by phase-mixing cannot belong to the FM mode.

Another feature we took into account to identify the observed perturbation is the polarization. Since the wavevector of these perturbations is nearly parallel to the y direction, the condition $\nabla \cdot \mathbf{B} = 0$ implies that the dominant components are B_{1x} and B_{1z} . We considered these components in the polarization analysis. Equations (12) and (14) indicate that the magnetic perturbation is elliptically polarized. In particular, using the dispersion relation (5), we calculated the quantity

$$\sigma(\mathbf{k}, \beta_0) = 1 - \frac{\omega^2}{c_{A0}^2 k_{\parallel}^2} \quad (28)$$

appearing in equations (12) and (14). In Fig. 5 we report σ as a function of k_{\perp} for the three modes, for $k_{\parallel} = 1$ and for two values of β_0 , corresponding to the lateral uniform region ($\beta_0 = 2.08$) and to the middle of the shear layer ($\beta_0 = 1.25$). From Fig. 5 we see that σ is negative for Alfvén and FM waves, while is positive for SM waves. Then, for positive k_{\parallel} and k_{\perp} and given values of t and x , as one increases the y coordinate, the perturbation magnetic field rotates clockwise (counterclockwise) in the zx plane for Alfvén and FM waves (SM waves). This characteristic behavior of the eigenmodes has been compared with the simulation results.

In Fig. 6 we plot a hodogram in the δB_x - δB_z plane, parameterized by the coordinate y which varies in the range $[\pi, 2\pi]$. This sample is for a fixed value of the x -coordinate $x = \pi$, and at the time $t = 20$. At that time, the perturbation generated inside the shear layer almost fill the lateral uniform region. In the hodogram the blue diamonds indicate the shear

layer ($4 \leq y \leq 5$) while red triangles indicate the lateral uniform region ($5 \leq y \leq 2\pi$). The blue asterisk indicates the central point $y = \pi$ and the red square indicates the boundary $y = 2\pi$. It is seen that in most of the shear layer and in the lateral homogeneous region the perturbed magnetic field clockwise turns with increasing y . Since in this region k_y is positive, the observed polarization in the simulation is in accordance with that of the Alfvén branch.

In conclusion, based both on the group velocity and on the polarization analysis, we deduce that the fluctuations generated inside the shear layers are KAWs. From the hodogram we also notice that the perturbation amplitude in the shear layer is smaller than in the lateral uniform region. Then, the process of KAW generation and their subsequent lateral propagation tends to move the initial Alfvén wave energy away from the shear regions. A process of local fluctuating energy depletion is eventually found also in the pure MHD case, but it is simply due to dissipation localized at the shear layers.

In the hodogram of Fig. 6 a small perturbation can be seen at the boundary between the shear layer and the inner homogeneous region, in which the magnetic field counterclockwise turns. This can be interpreted as a SM perturbation propagating from the shear layer toward the central region, i.e., opposite to k_y , as predicted by the linear theory (see Fig. 1). This SM perturbation can be seen also in Fig. 4 as a fluctuation drifting toward the center $y = \pi$ of the domain. However, the energy associated with this perturbation is much lower than that of the fluctuation that we have identified as a KAW.

4. Large-amplitude HMHD and kinetic simulations

Next, we consider the phase-mixing of an initial large-amplitude ($a = 0.25$) Alfvén wave. We show results from both a HMHD (RUN 3) and a kinetic (RUN 4) simulation.

The results are qualitatively similar as in the small-amplitude case, as it can be seen in Fig. 7 where $\delta B_x(x, y)$ is illustrated in the x, y -plane for the four runs at time $t = 13.1$. In particular, also in the large-amplitude case phase-mixing of the initial wave generates small scale variations perpendicular to $\mathbf{B}^{(0)}$ in the shear layers, mainly in the form of KAWs. The identification of these waves employs the same method as in the low-amplitude case, namely, considering both the perpendicular group velocity of perturbations and their polarization. The main difference between the low and high-amplitude case is that in the latter a small-amplitude precursor of the main KAW perturbation is observed to fill the lateral homogeneous region before the arrival of the main perturbation (Fig. 7).

The kinetic simulation (RUN 4) has been performed using a HVM numerical code (Valentini et al., 2007). The HVM algorithm integrates numerically the Vlasov equation for the proton distribution function in multi-dimensional phase space. In the present work, we restrict our analysis to the 2D-3V (two dimensions in physical space and three dimensions in velocity space) phase space configuration. The electrons are considered as a fluid and a generalized Ohm equation is employed for computing the electric field, which retains the Hall term. In the present work electron inertia effects are neglected. Quasi neutrality is assumed and the displacement current is neglected in the Ampere equation, therefore assuming low frequency dynamics. Finally, an isothermal equation of state for a scalar electron pressure is employed to close the HVM system. The equations solved by the HVM code are the following:

$$\frac{\partial f}{\partial t} + \mathbf{u} \cdot \nabla f + \frac{1}{\tilde{\epsilon}} (\mathbf{E} + \mathbf{u} \times \mathbf{B}) \cdot \frac{\partial f}{\partial \mathbf{u}} = 0 \quad (29)$$

$$\mathbf{E} = -\mathbf{v} \times \mathbf{B} + \frac{\tilde{\epsilon}}{n} \left(\mathbf{j} \times \mathbf{B} - \frac{\tilde{\beta}}{2} \nabla P_e \right) \quad (30)$$

$$\frac{\partial \mathbf{B}}{\partial t} = -\nabla \times \mathbf{E} \quad ; \quad \nabla \times \mathbf{B} = \mathbf{j} \quad (31)$$

where $f(x, y, u_x, u_y, u_z, t)$ is the proton distribution function in phase space and $\mathbf{E}(x, y, t)$ is

the electric field. The proton density n and the ion bulk velocity \mathbf{v} are obtained as velocity moments of f . The scalar electron pressure P_e is derived from an isothermal equation of state assuming that the electron temperature is equal to the initial (uniform) proton temperature. In equations (29)-(31) all quantities are dimensionless, as specified for the HMHD equations (1)-(4); moreover, the velocity \mathbf{u} is normalized to \tilde{c}_A , the density n to $\tilde{\rho}/m_p$, the electric field \mathbf{E} to $\tilde{c}_A\tilde{B}/c$, and the current density \mathbf{j} to $c\tilde{B}/(4\pi\tilde{L})$. A detailed description of the numerical method employed to solve equations (29)-(31) can be found in Valentini et al., (2007). The 2D-3V phase space has been discretized (see table 1) with $n_x \times n_y = 256 \times 1024$ grid points in the spatial domain and 51^3 grid points in the velocity domain.

The initial and boundary conditions (in the physical space) used in RUN 4 are the same as those used in the previous large-amplitude HMHD run (RUN 3). In the 3D velocity domain, the distribution function f is set equal to zero for $|\mathbf{u}| > u_{max}$, where $u_{max} = 5v_{th,p}$ and $v_{th,p}$ is the proton thermal speed. Moreover, the initial unperturbed proton distribution function is a Maxwellian with a uniform temperature $T^{(0)} = 0.5$. From Fig. 7 one can observe that the fluctuations δB_x obtained from the HVM run (RUN 4) at time $t = 13.1$ are similar to those seen in the HMHD run (RUN 3): KAWs develop in the shear layers and slowly drift toward the lateral uniform region. This similarity is probably related to the fact that both models (HMHD and HVM) employ the same form for the Ohm's law. In Fig. 8, we compare the power spectra of $\ln|\delta B|^2$ from RUN 3 (left panel) and RUN 4 (right panel), at the time $t = 13.1$. The contour plots in this figure display similar features, i.e. marked anisotropy along the k_y direction due to the phase-mixing process, but we can notice that more energy has transferred into small scales in RUN 4 relative to RUN 3. This suggests the presence of enhanced small-scale activity when kinetic effects are retained in the description of the plasma dynamics.

The ion microscopic dynamics which is described by the HVM model introduces evidently new effects with respect to the HMHD model, which are described in the following. First, we notice that the amplitude of δv_x at $t = 13.1$ is much lower in RUN 4 than in RUN 3. This difference can be better appreciated in Fig. 9, where profiles of δv_x at as a function of y at $x = \pi$ and at two different times are plotted. It can be seen that the amplitude of δv_x , which is initially vanishing, increases in time in the HMHD run, while it remains at a much lower level in the HVM run. Such a different behavior is presumably due to kinetic damping effects in RUN 4 that act on velocity fluctuations parallel to the background magnetic field; such damping mechanisms are absent in HMHD.

The HVM models allows us to follow how the proton distribution function is distorted, due to resonant interaction of protons with the KAW fluctuations, at different space positions and times with respect to the initial Maxwellian (in contrast, the HMHD model assumes local thermodynamic equilibrium). To characterize the departure of the computed f from a Maxwellian distribution, we define an L^2 -norm difference (Greco et al. 2012; Valentini et al. 2014):

$$\varepsilon(x, y, t) = \frac{1}{n} \sqrt{\int [f(\mathbf{x}, \mathbf{u}, t) - M(\mathbf{x}, \mathbf{u}, t)]^2 d^3 \mathbf{u}} \quad (32)$$

where M is a Maxwellian with the same density, bulk velocity and isotropic temperature as f . ε is a positive definite quantity and may be viewed as a “distance” or separation between the computed f and an equivalent Maxwellian. In Fig. 10 the maximum

$$\varepsilon_{max}(t) = \max_{(x,y) \in D} \varepsilon(x, y, t) \quad (33)$$

is plotted as a function of time. We see that ε_{max} increases in time, eventually saturating at a value $\simeq 0.035$; this indicate a progressive departure from a Maxwellian distribution. In Fig. 10 the time t_d is indicated as a vertical red-dashed line, corresponding to the time necessary for phase-mixing to produce transverse wavevectors comparable with \tilde{d}_p^{-1} . At

$t \sim t_d$ the growth of ε_{max} becomes slower, indicating that the largest departure from a Maxwellian is almost reached when fluctuations at scales of the order of the proton inertial length are formed. This is an indication that the KAW fluctuations are responsible for the modifications in the proton distribution function. Another quantity describing the departure of f from a Maxwellian is the temperature anisotropy parameter (Perrone et al. 2013)

$$R(x, y, t) = 1 - \frac{T_{p\perp}(x, y, t)}{T_{p\parallel}(x, y, t)} \quad (34)$$

where $T_{p\perp}$ and $T_{p\parallel}$ are the proton temperature perpendicular and parallel to the local magnetic field \mathbf{B} , respectively; $R < 0$ ($R > 0$) corresponds to $T_{p\perp}$ larger (smaller) than $T_{p\parallel}$. From results of RUN 4 we found that ε and $|R|$ are clearly correlated, the correlation coefficient being $\simeq 0.74$. This indicates that the departures of f from a Maxwellian are essentially due to the generation of temperature anisotropy. In Fig. 11 the spatial distributions of R (left) and ε (middle) are plotted at the time $t = 13.1$, together with the parallel electric field (right); comparing with Fig. 7 we see that the largest departures from a Maxwellian are spatially correlated with KAWs, i.e., with fluctuations at transverse scales comparable with d_p . Positive and negative variations of the anisotropy parameter R with similar amplitudes follow one another along the KAW profile. Then, a prevalence of parallel or perpendicular proton kinetic energy can equally take place, due to interactions with KAWs, according to the wave phase. A 3D representation (surface plot) of the proton velocity distribution at time $t = 13.1$ is shown in the top row of Fig. 12, for two different spatial locations: $(x, y) = (5.4, 1.5)$ (left), where R is minimum at the given time, i.e., $T_{p\perp} > T_{p\parallel}$, and $(x, y) = (6.2, 4.7)$ (right), where ε is maximum and $T_{p\perp} < T_{p\parallel}$. As it is clear from these two plots, both distributions depart from a spherical shape, typical of a Maxwellian distribution, and display a structuring in the form of rings perpendicular to the local magnetic field, indicating groups of particles in resonance with large-amplitude fluctuations. In the bottom row of the same figure, the contour plots (together with the level

lines) of the proton velocity distribution in the u_x - u_y plane (for $u_z = 0$) are presented at the same time and spatial locations as for the top row plots. In particular, the bottom-right panel, corresponding to the location where the ratio $T_{p\parallel}/T_{p\perp}$ is particularly large, shows the presence of a well-defined beam of ions moving in the direction parallel to the local magnetic field. Such a beam is spatially localized where the KAW fluctuations have been generated by phase-mixing, and therefore it is reasonable to postulate that the beam is produced by a wave-particle interaction between protons and the fluctuations that we have characterized as KAWs.

Such interaction could be related to the fluctuating parallel electric field δE_{\parallel} associated with the KAW. In fact, the Ohm's law (30) allows for the presence of an electric field component $E_{\parallel} = \mathbf{E} \cdot \mathbf{B}/B$ parallel to the magnetic field. This component is due to the electron pressure gradient term in equation (30). In Fig. 11 E_{\parallel} is plotted at time $t = 13.1$. It can be seen that a fluctuation $\delta E_{\parallel} \sim 10^{-2}$ forms mainly in the shear layers, where KAWs are localized. The presence of parallel electric field fluctuations is another feature characterizing KAWs. In the ideal HMHD case E_{\parallel} has no effects on the dynamics (the term containing $\nabla P_e/n$ being canceled out when calculating $\nabla \times \mathbf{E}$), unless one includes also a resistivity. However, in the HVM model it can have an influence on the evolution of the proton distribution function. In order to investigate this possibility, we considered the potential energy variation (per particle) δU associated with δE_{\parallel} , in comparison with the proton thermal energy E_{th} . The ratio between these two quantities, expressed in our normalized units, can be estimated as:

$$\frac{\delta U}{E_{th}} \sim \frac{8}{3\tilde{\epsilon}\tilde{\beta}} \frac{\delta E_{\parallel}\lambda_{\parallel}}{T_p} \quad (35)$$

where λ_{\parallel} is the parallel wavelength and T_p is the proton temperature. Using the values $\tilde{\epsilon} = 0.125$, $\tilde{\beta} = 2$, $\delta E_{\parallel} \sim 10^{-2}$, $\lambda_{\parallel} = 2\pi$, and $T_p \sim 0.5$, from equation (35) we find $\delta U/E_{th} \sim 1$. Then, the potential energy variation associated with the parallel electric field

associated with the KAWs is comparable to the proton thermal energy. This implies that δE_{\parallel} is able to sensibly modify the initial proton distribution function. Moreover, the velocity of the proton beam is $u_{beam} \simeq 1.8$. We measured the phase velocity of the perturbation along x , finding $w_x \simeq 1.6$ which is comparable with u_{beam} . These considerations strongly suggest that the observed field-aligned particle beam is generated by the resonant interaction of protons with the parallel electric field δE_{\parallel} associated with the KAW fluctuations.

5. Discussion and conclusions

In this paper we have shown that fluctuations having the character of oblique Kinetic Alfvén Waves are readily generated using a simple configuration consisting of an in-plane two dimensional sheared magnetic field, and an out-of-plane perturbation that locally propagates as an Alfvén wave. We have described the emergence of the KAWs as occurring due to phase-mixing, or refraction of the perturbation wave vectors towards angles highly oblique with respect to the sheared magnetic field direction. Although the refraction is seen in MHD (Ghosh et al. 1998), the basic physical picture of the emergence of KAWs requires at least a model as complete as HMHD, where it is seen at both low and high initial perturbation amplitudes when the thickness of perturbation across the magnetic field becomes comparable with the proton skin depth. For the case of a Hybrid Vlasov solution, at this stage additional features are observed during this process, such as non-Maxwellian proton distributions, temperature anisotropy, and the formation a parallel beam in the proton velocity distribution. Evidence for resonant wave-particle interaction between the beam and the KAW perturbation is also identified.

The simplicity of the initial setup adopted in these numerical experiments made it possible to characterize features of KAWs in several ways. These included, for example, examination of wave polarizations and phase speeds based on linear theory. The

identification was facilitated by the choice of the magnetic shear as an ideal MHD, HMHD and HVM equilibrium, as well as the choice of perturbation as an Alfvén mode. However, it is equally important to recognize that much of the physical picture described in this idealized context is expected to carry over to more complex configuration, including even a full quasi-incompressible turbulence cascade. To elaborate on this point briefly we note that incompressible couplings, such as those that dominate the present models, correspond to quadratic terms, for example in the MHD equations (Eqs (2) and (3)) written for constant density. These nonlinear couplings (we are speaking here of the equations prior to separation into equilibrium and perturbation) have the familiar property that the Fourier amplitude with wave vector \mathbf{k} may interact directly with two other wave vectors \mathbf{p} and \mathbf{q} provided that the triadic condition $\mathbf{k} = \mathbf{p} + \mathbf{q}$ is satisfied. Suppose we identify the sheared magnetic field in Eq. (19) as $\mathbf{B}^{(0)} = (B^{(0)}(y), 0, 0)$ having Fourier modes at wavevectors $\mathbf{p} \rightarrow (0, p_y, 0)$. Now let the perturbation consist of wave vectors \mathbf{q} and require that it be of an incompressible type but otherwise relax the restrictions of the special case given in Eq. (24). It is immediately clear that even in a large amplitude situation more complex than what we treated above, the triadic nonlinear couplings will drive excitations to wavevectors $\mathbf{k} = (0, p_y, 0) + (q_x, q_y, q_z)$ that will acquire increasing values of k_y . That is the fluctuations will spectrally transfer towards wavevectors that are oblique to the sheared magnetic field direction. This is closely related to the standard argument (Shebalin et al. 1983) for perpendicular spectral transfer, and is very similar to the nonlinear phase-mixing associated with velocity shears and pressure balance structures seen in MHD turbulence simulations with analogous initial setups (Ghosh et al. 1998). In this way we can see that the driver of the refraction towards highly oblique wave vectors is considerably more general than in the special case we considered here. It is reasonable to suppose then, that the Hall and kinetic effects that we identified as emerging when the transverse scales decrease to the ion inertial length will also be observed in these more complex circumstances.

We can conclude then that the simple mechanism we described here in the context of HMHD and Hybrid Vlasov models provides a pathway to understand generation of fluctuations with the character of Kinetic Alfvén Waves. Driven by magnetic shear, the excitations appear at ever smaller scales across the magnetic shear layer until the Hall/kinetic effects appear near the ion inertial length scale. Analysis of polarization and propagation speed identifies these fluctuations as being of the KAW-type. Particularly interesting is the emergence of a field-aligned beam in the self-consistent proton distribution function, apparently admitting signatures of wave-particle resonances. We conjecture that the mechanism described here operates also in a quasi-incompressible cascade scenario, so that the basic reasoning given here may also account for emergence of KAW-like features at proton kinetic scales in strong turbulence, as suggested based on solar wind observations (Bale et al. 2005; Sahraoui et al. 2012).

The authors are grateful to P. Veltri for many stimulating discussions on the subject of the paper. Thanks are due to O. Pezzi for useful suggestions in the analytical treatment of the linear problem and to T. Alberti for valuable help with simulation data reduction. The numerical HVM simulations have been running on the Fermi supercomputer at CINECA (Bologna, Italy), within the ISCRA-C project IsC26-PMKAW. WHM was partially supported by NASA Grand Challenge Research project NNX14AI63G and by NSF AGS-1063439 and AGS-1156094.

REFERENCES

- Bale, S. D., Kellog, P. J., Mozer, F. S., Horbury, T. S. & Reme, H. 2005, *Phys. Rev. Lett.*, 94, 215002
- Barnes, A. 1979, *Space Plasma Physics: The Study of Solar-System Plasmas*. (National Academy of Sciences, Washington, DC USA), Volume 2, 257
- Belcher, J. W., & Davis, L. 1971, *J. Geophys. Res.*, 76, 3534
- Birkhoff, G., & Mac Lane, S., *A survey of Modern Algebra*, 4th Ed. (Macmillan Publishing Co., Inc, New York, NY, 1977) pp. 118-120.
- Bruno, R., & Carbone, V. 2005, *Living Rev. Solar Phys.*, 2, 4
- Califano, F., Chiuderi, C., & Einaudi, G. 1990, *ApJ*, 365,757
- Califano, F., Chiuderi, C., & Einaudi, G. 1992, *ApJ*, 390,560
- Carbone, V., & Veltri, P. 1990, *Geophys. Astrophys. Fluid Dynamics*, 52, 153
- Chen, C. H. K., Boldyrev, S., Xia, Q., & Perez, J. C. 2013, *Phys. Rev. Lett.*, 110, 225002
- Davila, J. M. 1987, *ApJ*, 317, 514
- Décamp, N., & Malara F. 2006, *Electron Acceleration in Turbulent Coronal Loops by Kinetic Alfvén Waves*, in "SOHO-17. 10 Years of SOHO and Beyond", H. Lacoste & L. Ouwehand Eds., ESA SP-61
- Donato, S., Servidio, S., Dmitruk, P., Carbone, V., Shay, M. A., Cassak, P. A., & Matthaeus, W. H. 2012, *Phys. Plasmas*, 19, 092307
- Gary, S. P., & Nishimura, K. 2004, *J. Geophys. Res.*, 109, A02109

- S. Ghosh, M. Hossain, and W. H. Matthaeus, *Computer Physics Communications* **74**, 18 (1993).
- Ghosh, S, Matthaeus WH, Roberts DA & Goldstein ML 1998, *J. Geophys. Res.* 103, 23691
- Greco A., Valentini F., Servidio S. & Matthaeus W. H. 2012, *Phys. Rev. E*, 86, 066405
- Heyvaerts, J., & Priest, E. R. 1983, *A&A*, 117, 220
- Hollweg, J. 1987, *ApJ*, 312, 880
- Hollweg, J., 1999, *J. Geophys. Res.* 104, 47
- Howes, G. G., Cowley, S. C., Dorland, W., Hammett, G. W., Quataert, E., Schekochihin, A. A., & Tatsuno, T. 2008a, *Phys. Rev. Lett.* 100, 065004
- Howes, G. G., Dorland, W., Cowley, S. C., Hammett, G. W., Quataert, E., & Schekochihin, A. A. 2008b, *J. Geophys. Res.* 113, A05103
- Kappraff, J. M., & Tataronis, J. A. 1977, *J. Plasma Phys.*, 18, 209
- Kiyani, K. H., Chapman, S. C., Sahraoui, F., Hnat, B., Fauvarque, O., & Khotyaintsev, Yu. V. 2013, *AstroPhys. J.* 763, 10
- Landi, S., Velli, M., & Einaudi, G. 2005, *ApJ*, 624, 392
- Lee, E. M., & Roberts, B. 1986, *ApJ*, 301, 430
- Lysak, R. L. & Song Y. (2011) *J. Geophys. Res.*, 116, A00K14 DOI:10.1029/2010JA016424
- Malara, F., Veltri, P., Chiuderi, C., & Einaudi, G. 1992, *ApJ*, 396, 297
- Malara, F., Primavera, L., & Veltri, P. 1996, *ApJ*, 459, 347
- Malara, F., Petkaki, P., & Veltri, P. 2000, *ApJ*, 533, 523

- Malara, F., De Franceschis, M. F., & Veltri, P. 2003, *A&A*, 412, 529
- Malara, F., De Franceschis, M. F., & Veltri, P. 2005, *A&A*, 443, 1033
- Malara, F., Veltri, P., & De Franceschis, M. F. 2007, *A&A*, 467, 1275
- Matthaeus, W. H., Goldstein, M. L., & King, J. H. 1986, *J. Geophys. Res.*, 91, 59
- Matthaeus, W. H., Goldstein, M. L., & Roberts, D. A. 1990, *J. Geophys. Res.*, 95, 20673
- Matthaeus, WH Wan, M., Servidio, S; Greco, A., Osman, KT; Oughton, S & Dmitruk, P
2015, *Phil. Tans Roy Soc A*, 373, 20140154, DOI:10.1098/rsta.2014.0154
- McLaughlin, J. A., Hood, A. W., & De Moortel, I. 2010, *Space Sci. Rev.*, doi:10.1007/s11214-010-9654-y
- Mok, Y., & Einaudi, G. 1985, *J. Plasma Phys.*, 33, 199
- Nakariakov, V. M., Roberts, B., & Murawski, K. 1997, *Sol. Phys.*, 175, 93
- Nakariakov, V. M., Roberts, B., & Murawski, K. 1997, *A&A*, 332, 795
- Ofman L. & Aschwanden M. J. (2002) *Astrophys. J.*, 576 L153
- Oughton, S., Priest, E. R. & Matthaeus W. H. 1994, *J. Fluid Mech.*, 280, 95
- Perrone D., Dendy R. O., Furno I., Sanchez R., Zimbardo G., Bovet A., Fasoli A., Gustafson
K., Perri S., Ricci P & Valentini F. 2013, *Space Sci Rev*, 178, 233
- Petkaki, P., Malara, F., & Veltri, P. 1998, *ApJ*, 500, 483
- Podesta, J. J., & Tenbarge, J. M. 2012, *J. Geophys. Res.* 117, A10106
- Ruderman, M. S., Nakariakov, V. M., & Roberts, B. 1998, *A&A*, 338, 1118

- Sahraoui, F., Goldstein, M. L., Robert, P., & Khotyaintsev, Yu. V. 2009, *Phys. Rev. Lett.* 102, 231102
- Sahraoui, F., Belmont, G., & Goldstein, M. L. 2009, *ApJ*, 748, 100
- Salem, C. S., Howes, G. G., Sundkvist, D., Bale, S. D., Chaston, C. C., Chen, C. H. K., & Mozer, F. S., *ApJ*, 745, L9
- Schekochihin, A. A., Cowley, S. C., Dorland, W., Hammett, G. W., Howes, G. G., Quataert, E., & Tatsuno, T. 2009, *ApJ*, 182, 310
- Shebalin, J. V., Matthaeus, W. H., & Montgomery, D. 1983, *J. Plasma Phys.*, 78, 2088
- Similon, P. L., & Sudan, R. N. 1989, *ApJ*, 336, 442
- Steinolfson, R. S. 1985, *ApJ*, 295, 213
- TenBarge, J. M., & Howes, G. G. 2012, *Phys. Plasmas* 19, 055901
- Tomczyk, S., McIntosh, S. W., Keil, S. L., Judge, P. G., Schad, T., Seeley, D. H., & Edmondson, J. 2007 *Science* 317, 1192
- Tomczyk, S., & McIntosh, S. W. 2009, *ApJ*, 697, 1384
- Tsiklauri, D., & Nakariakov, V. M. 2002, *A&A*, 393, 321
- Tsiklauri, D., Nakariakov, V. M., & Rowlands, G. 2003, *A&A*, 400, 1051
- Tsiklauri, D., Sakai, J.-I., & Saito S. 2005, *A&A*, 435, 1105
- Tsiklauri, D. 2011, *Phys. Plasmas*, 18, 092903
- Tsiklauri, D. 2012, *Phys. Plasmas*, 19, 082903

Valentini, F., Travnicek, P., Califano, F., Hellinger, P., Mangeney, A. 2007, *J. Comput. Phys.* 225, 753 (see also www.fis.unical.it/hvm).

Valentini F., Servidio S., Perrone D., Califano F., Matthaeus W. H. & Veltri P. 2014, *Physics of Plasmas*, 21, 082307

Vásconez, C. L., Valentini, F., Camporeale, E. & Veltri P. 2014, *Phys. Plasmas*, 21, 112107

Voitenko, Y., & Goossens, M. 2004, *ApJ*, 605, L149

Wu, D. J., & Chen, L. 2013, *ApJ*, 771:3

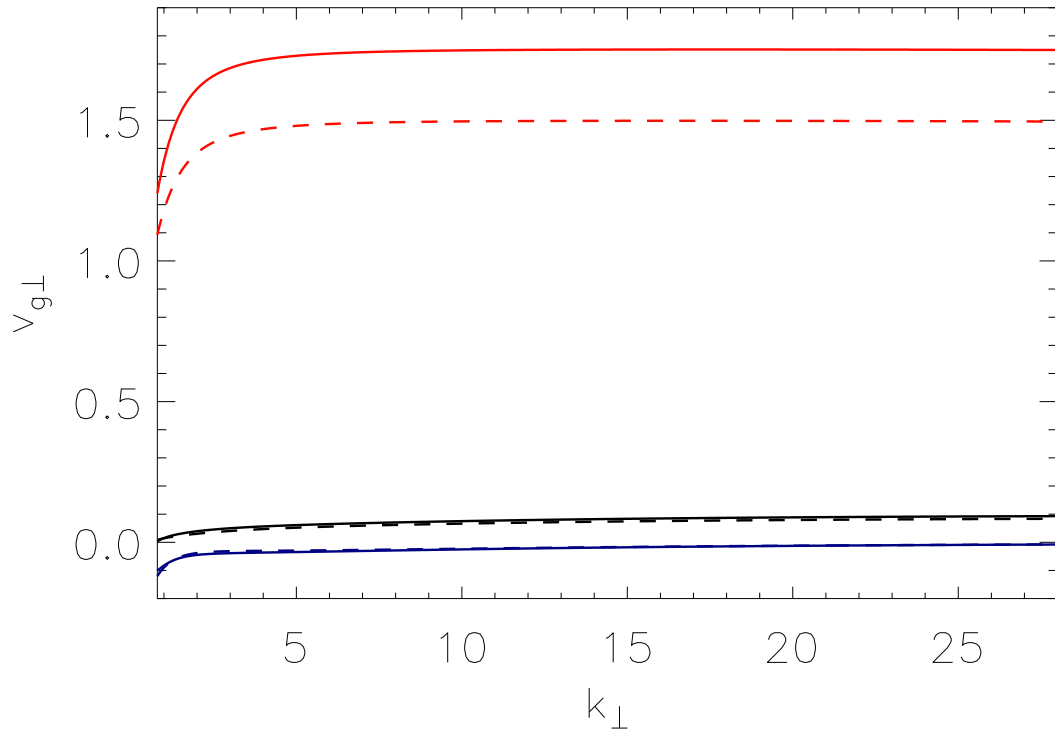


Fig. 1.— The perpendicular group velocity $v_{g\perp}$ of the Alfvén (black lines), FM (red lines) and SM (blue lines) modes is plotted as a function of k_{\perp} , for $k_{\parallel} = 1$ and for $\beta_0 = 2.08$ (full lines) and $\beta_0 = 1.25$ (dashed lines).

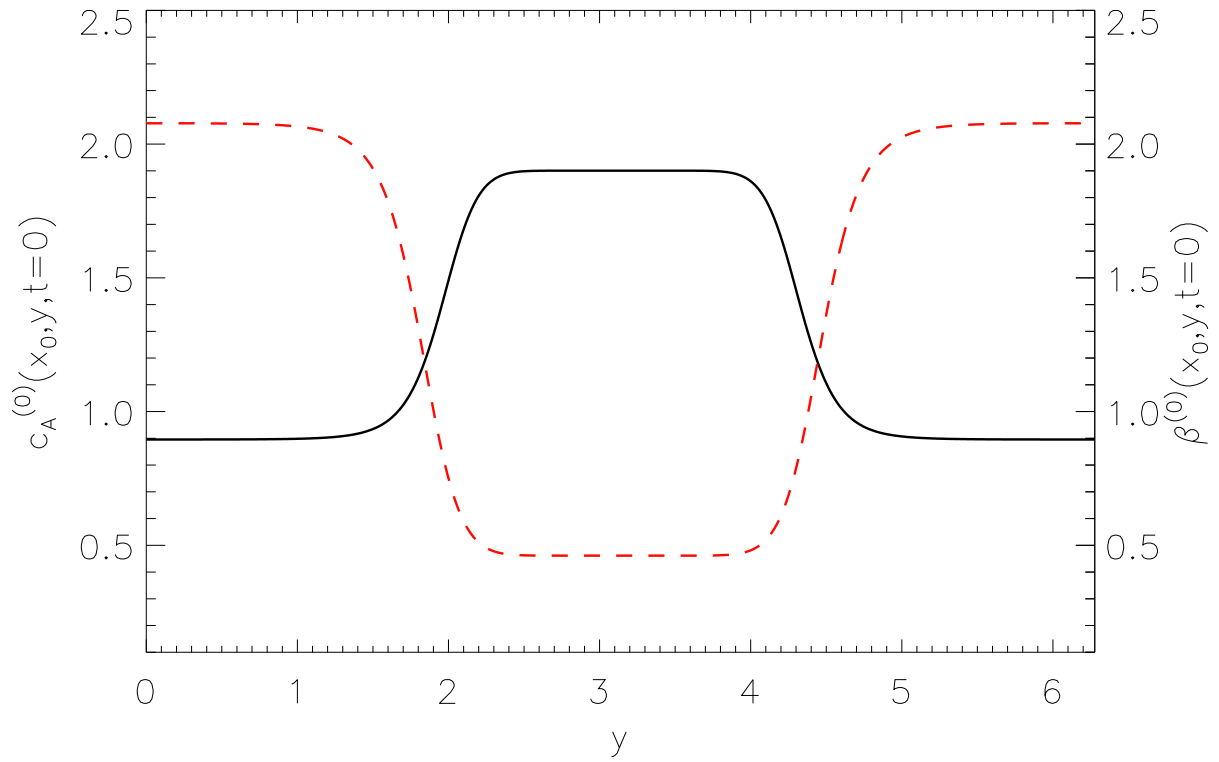


Fig. 2.— The Alfvén velocity $c_A^{(0)}$ (black solid line) and $\beta^{(0)}$ (red dashed line) associated with the equilibrium structure are plotted as functions of the y coordinate.

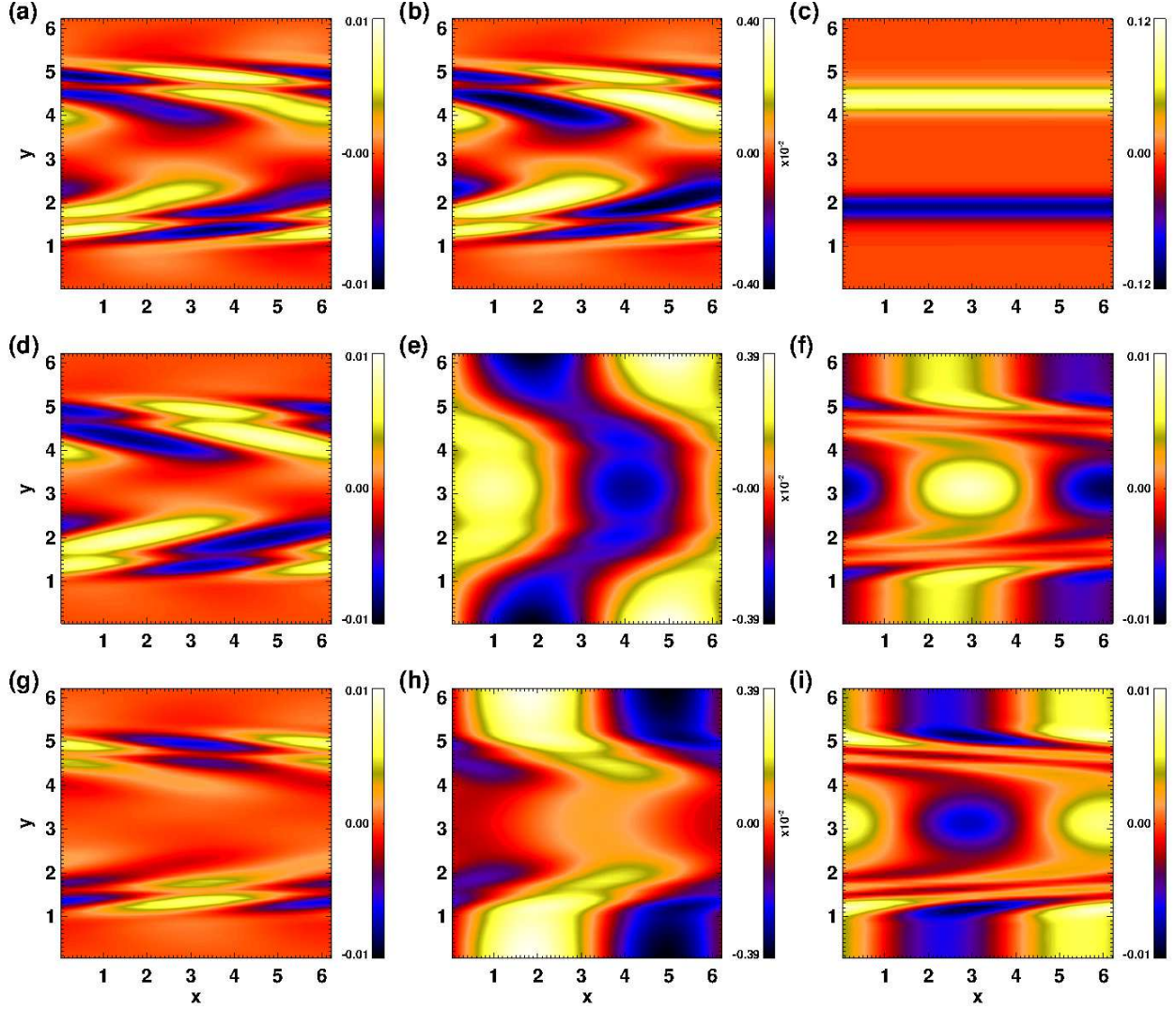


Fig. 3.— $\delta\rho$ (a), δT (b), j_z (c), δv_x (d), δv_y (e), δv_z (f), δB_x (g), δB_y (h), δB_z (i), plotted as functions of x and y , at the time $t = 13.1$ for the low-amplitude HMHD run (RUN 2).

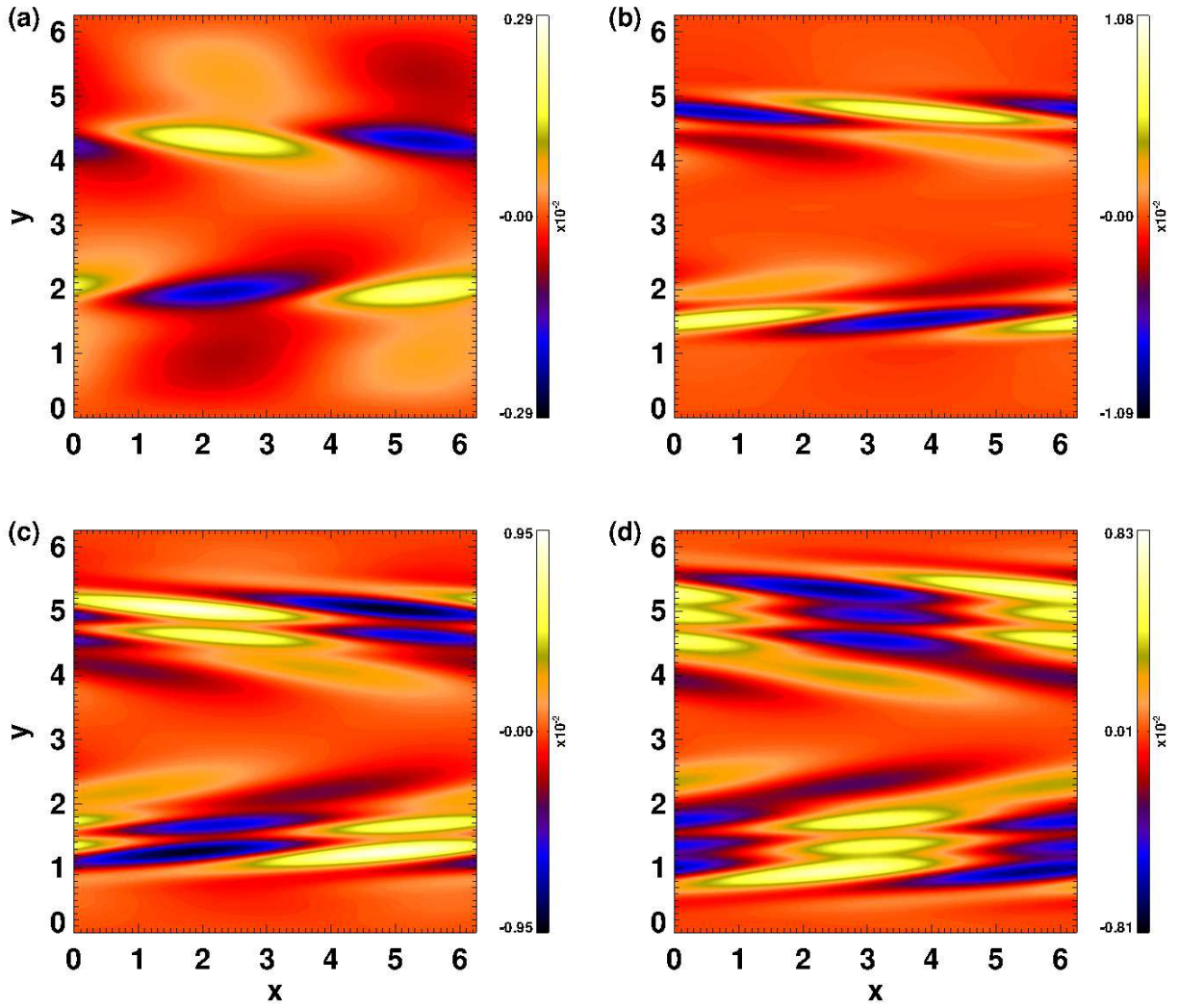


Fig. 4.— The δB_x component is plotted in the xy -plane at four different times for the low-amplitude HMHD run (RUN 2). $t = 2$ (a), $t = 10$ (b), $t = 15$ (c), $t = 20$ (d).

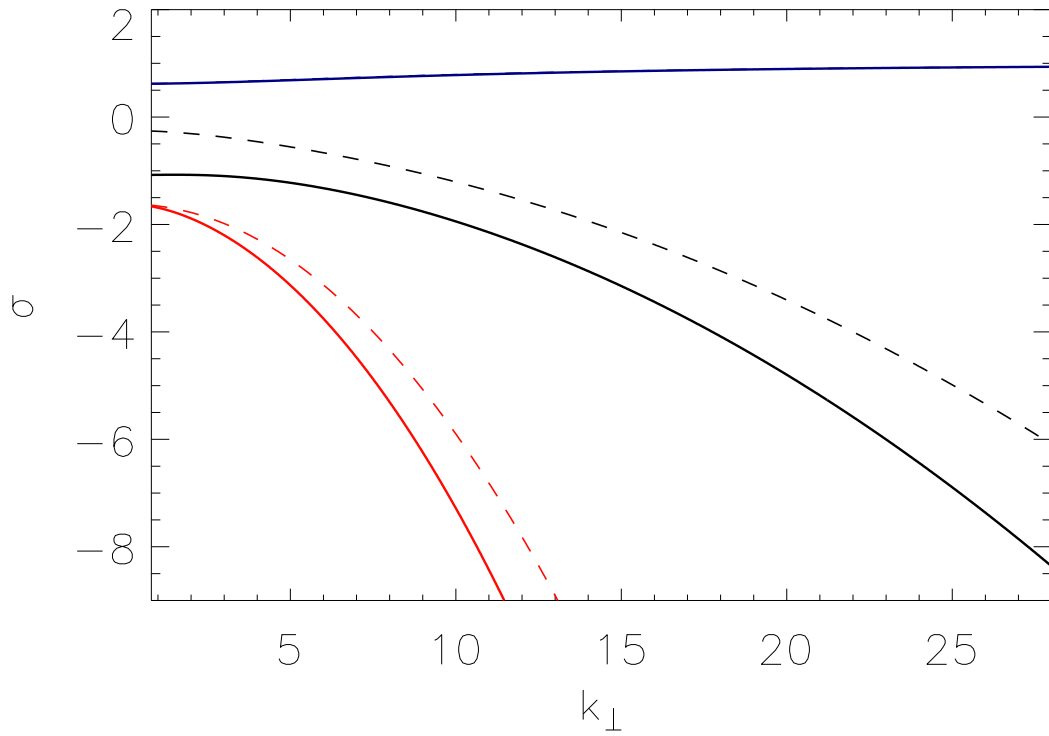


Fig. 5.— The quantity σ is plotted as a function of k_{\perp} , for $k_{\parallel} = 1$ and for $\beta_0 = 2.08$ (full lines) and $\beta_0 = 1.25$ (dashed lines). Black lines correspond to the Alfvén mode, red lines to the FM mode, and blue lines to the SM mode. In the latter case the curves corresponding to the two values of β_0 are superposed.

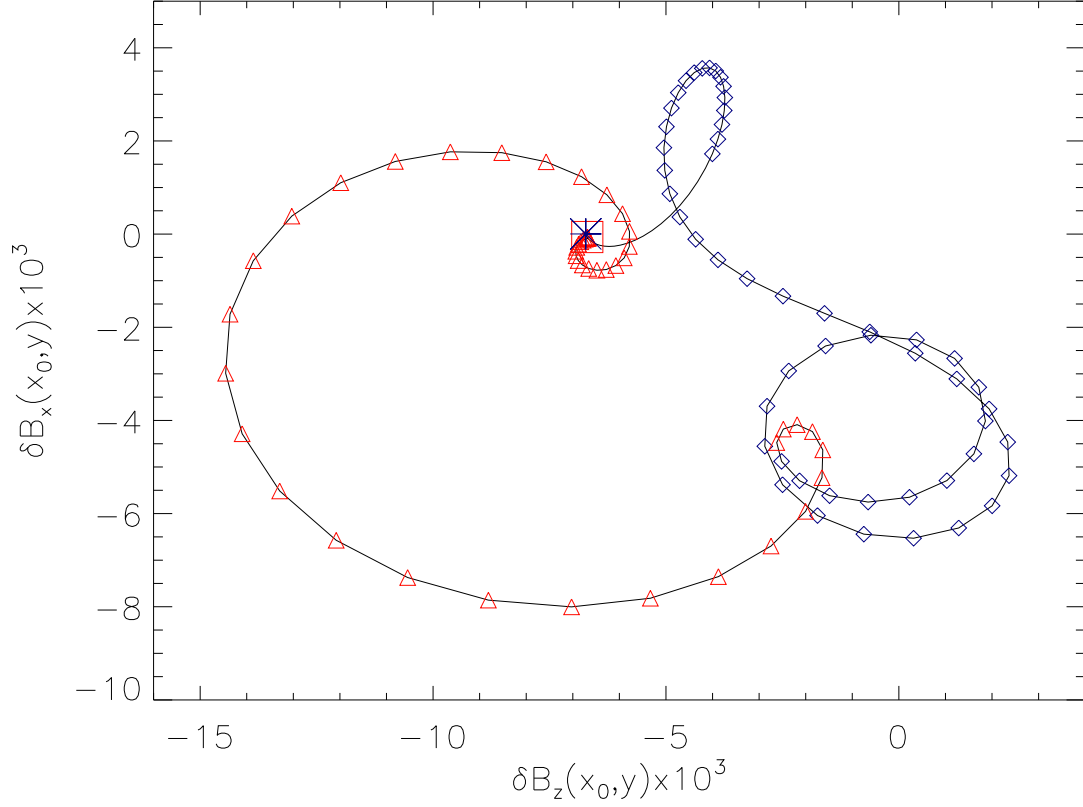


Fig. 6.— The δB_z and δB_x components are plotted on the two axes for y varying in the range $\pi \leq y \leq 2\pi$, at $x = x_0 = \pi$ and $t = 20$. The central point $y = \pi$ (blue asterisk), the boundary $y = 2\pi$ (red square), the shear layer region (blue diamonds), and the lateral homogeneous regions (red triangles) are indicated.

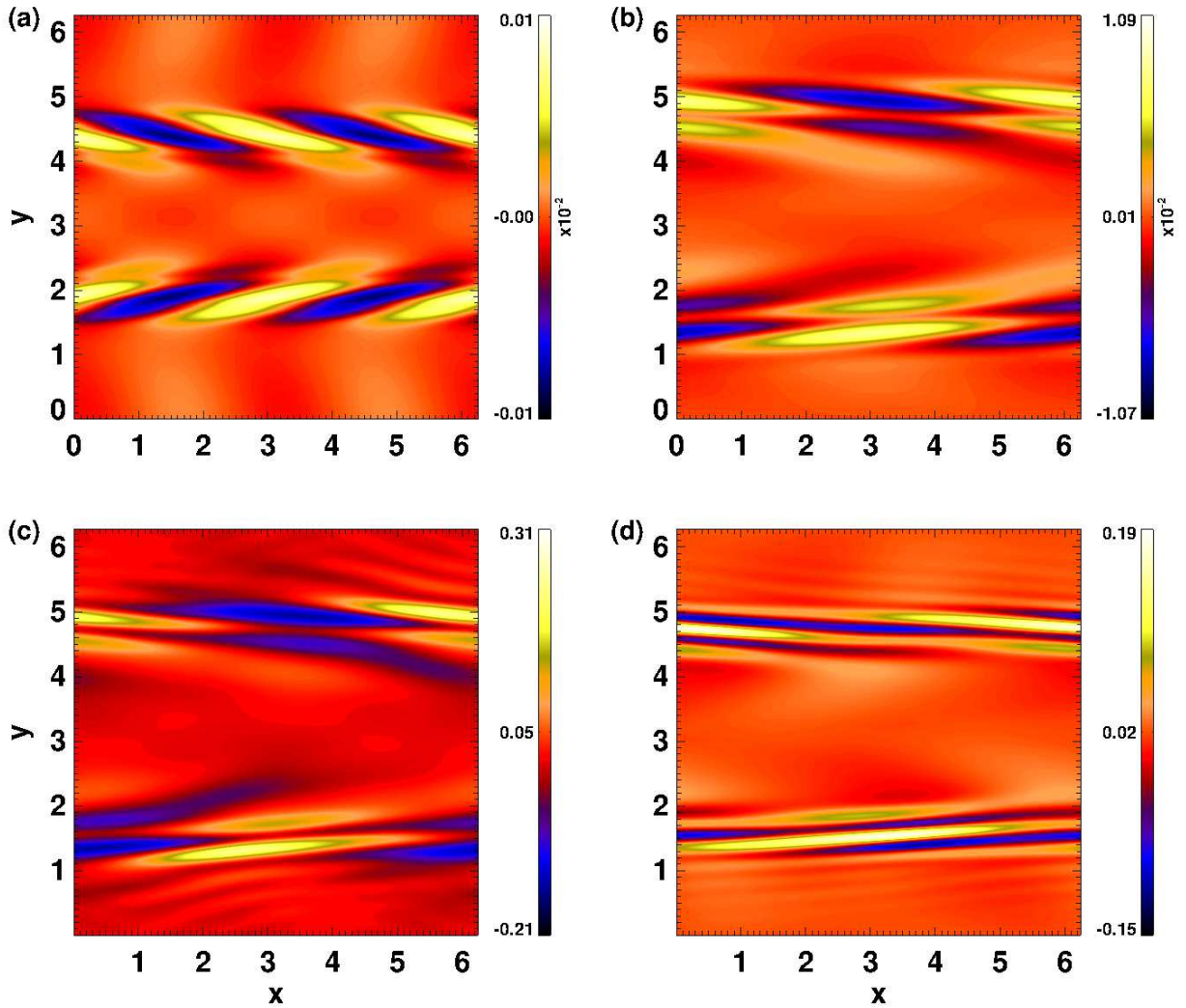


Fig. 7.— The component δB_x is plotted as function of x and y , at the time $t = 13.1$, for (a) RUN 1 - MHD with small a ; (b) RUN 2 - HMHD with small a ; (c) RUN 3 - HMHD, large a ; and (d) RUN 4 - HVM large a .

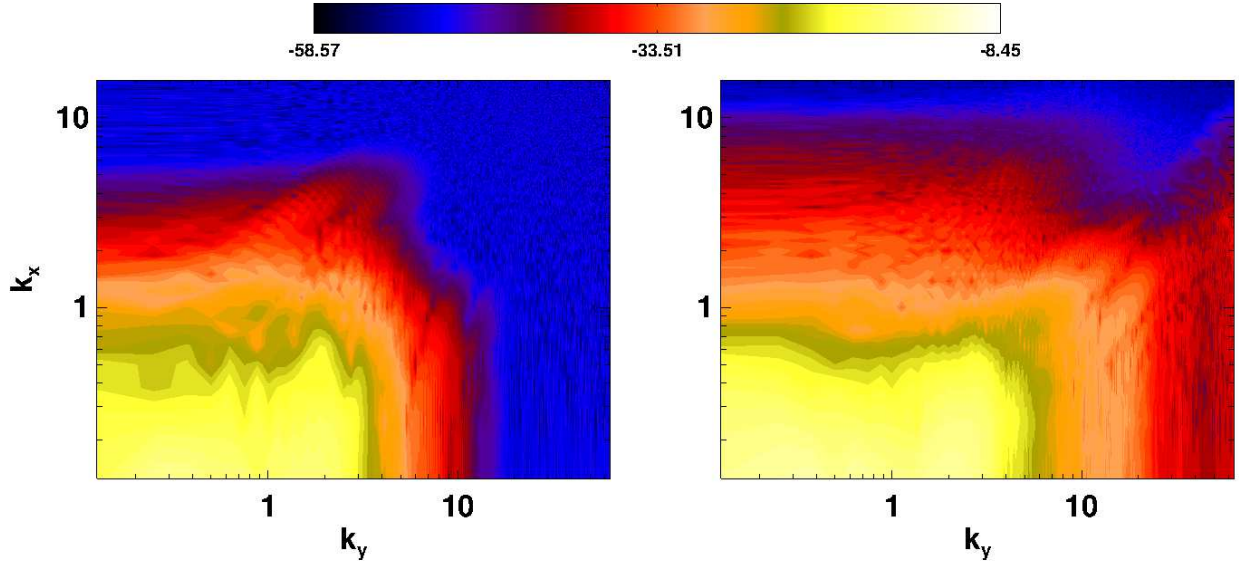


Fig. 8.— Power spectrum of $\ln |\delta B|^2$ from RUN 3 (left panel) and RUN 4 (right panel) at $t = 13.1$.

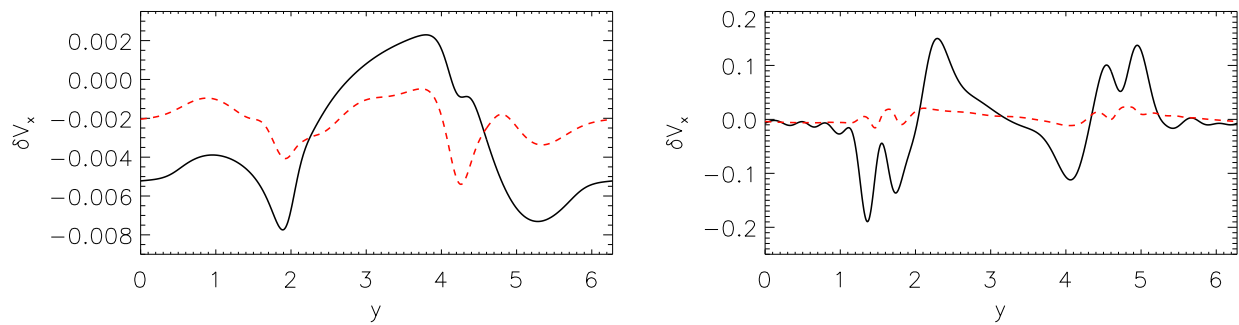


Fig. 9.— δv_x profiles are plotted as functions of y , for $x = \pi$, at times $t = 1$ (left panel) and $t = 13.1$ (right panel), for RUN 3 (black full line) and RUN 4 (red dashed line).

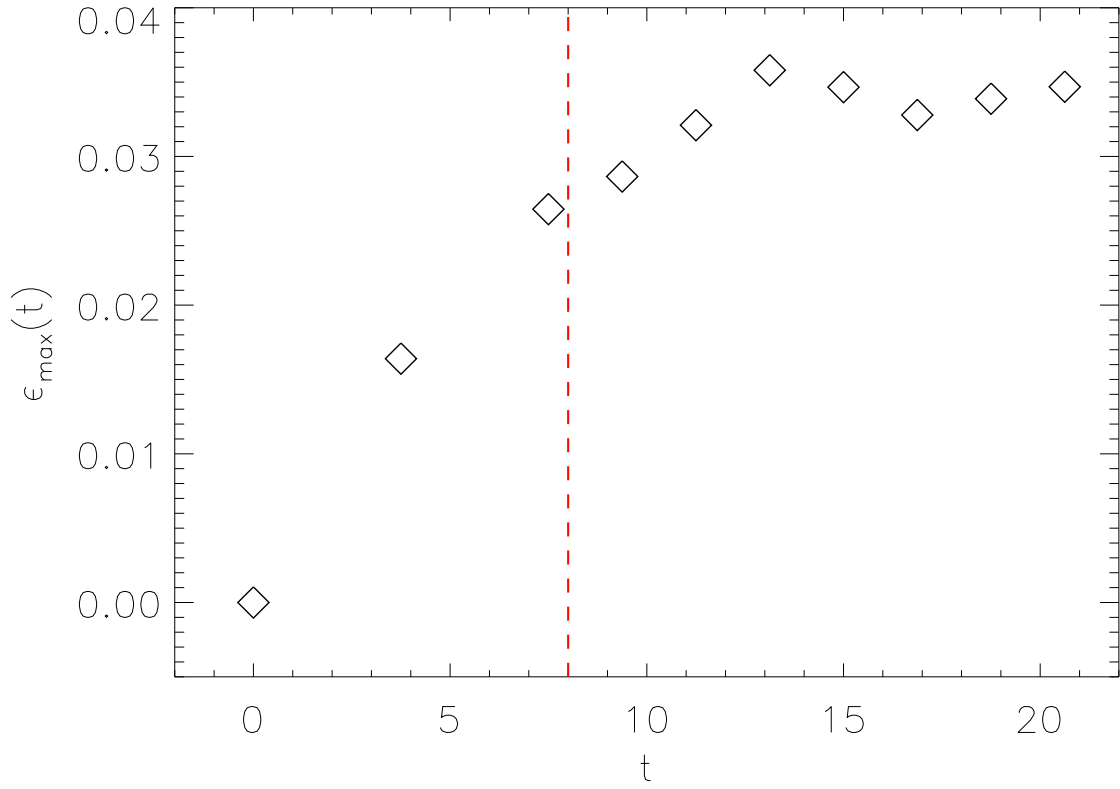


Fig. 10.— The quantity ϵ_{\max} , quantifying the departures of the HVM distribution function from a Maxwellian, is plotted as function of the time. The vertical dashed line indicates the time $t = t_d$, described in the text.

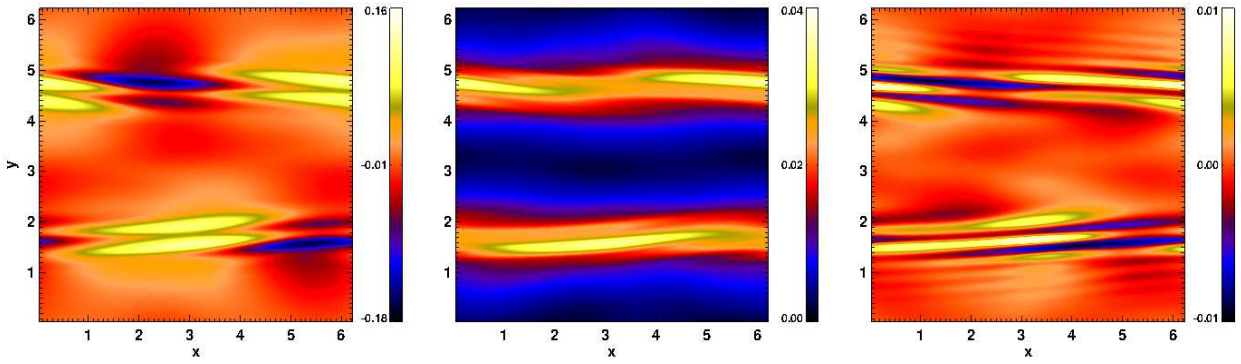


Fig. 11.— The quantities R (left panel), ε (middle panel), and the electric field parallel component $E_{||}$ (right panel) are plotted in the xy -plane, at time $t = 13.1$.

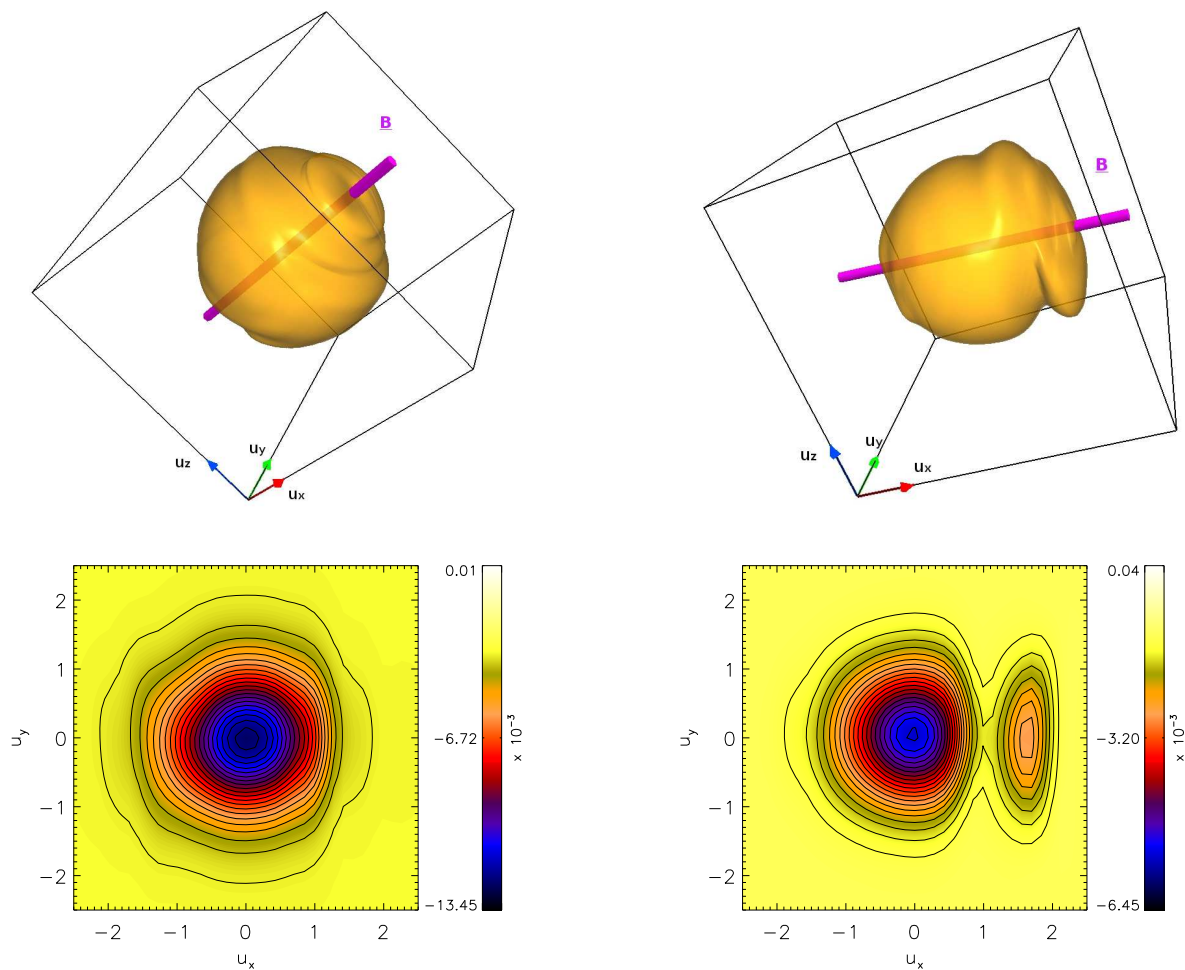


Fig. 12.— Top row: surface plot of the proton velocity distribution at the spatial location $(x, y) = (6.2, 4.7)$ (left), where ε is maximum and $T_{p\perp} < T_{p\parallel}$, and $(x, y) = (5.4, 1.5)$ (right) where R is minimum, i.e., $T_{p\perp} > T_{p\parallel}$. The magenta tubes in the two plots indicate the direction of the local magnetic field. Bottom row: shaded contours (together with level lines) of the proton velocity distribution, in the u_x - u_y plane (at $u_z = 0$), in the same spatial locations as in the top row.

Table 1: Simulations setup.

RUN	Type	Spatial Resolution ($n_x \times n_y$)	Amplitude (a)	Hall parameter ($\tilde{\epsilon}$)
1	MHD	256×256	0.01	0
2	HMHD	256×256	0.01	0.125
3	HMHD	256×1024	0.25	0.125
4	HVM	256×1024	0.25	0.125